NAVIER-STOKES CALCULATIONS FOR A HIGHLY-TWISTED ROTOR NEAR STALL

Gloria K. Yamauchi

Aerospace Engineer
NASA Ames Research Center, Moffett Field, CA

and

Wayne R. Johnson
Johnson Aeronautics, Palo Alto, CA

Summary

The viscous flow field near the surface of a hovering rotor blade was studied for blade twist distributions typical of a tilt rotor blade and a conventional helicopter rotor blade. Three blade geometries were studied, including a tilt rotor blade twist distribution (baseline), conventional helicopter rotor blade twist distribution, and the baseline twist distribution with 2 deg of precone. The results give insight into the delayed stall phenomenon often observed for highly twisted rotors. Calculations were performed for a high thrust condition near stall using the thin-layer Navier-Stokes CFD code TURNS. Effects of built-in twist on section force coefficients, skin friction, velocities, surface pressures, and boundary layer shape factor are discussed. Although the rotor thrust coefficient was nominally the same for the cases using the two twist distributions, large differences were found in the section in-plane and normal force coefficients. These preliminary results imply that the blade outboard region, rather than the inboard region, provides the majority of the performance advantage of the baseline case over the low twist case. Skin friction, velocities near the blade, and surface pressures for the two twist distributions reveal significant differences in the blade outboard region.

Notation

a_∞	freestream sound speed
c	chord
c_{ref}	reference chord, chord at 0.75 radial station (=25.075 in)
Cn	section normal force coefficient, section normal force/$(0.5\rho_\infty(\Omega r)^2 c)$
Cp	surface pressure coefficient, $(p-p_\infty)/(0.5\rho_\infty(\Omega r)^2)$
Ct	section thrust coefficient, section thrust/$(0.5\rho_\infty(\Omega R)^2 c_{ref})$
Cx	section in-plane force coefficient, section in-plane force/$(0.5\rho_\infty(\Omega R)^2 c_{ref})$
CT	rotor thrust coefficient, rotor thrust/$(\pi R^2\rho(\Omega R)^2)$
j,k,ℓ	grid indices
ℓe	grid point in blade normal direction defining boundary layer edge
H	boundary layer shape factor, δ^*/θ
M_{tip}	blade tip Mach number, $\Omega R/a_\infty$
p_∞	free stream static pressure
r	blade radial coordinate, radial location/R
R	blade radius (=19 ft)
Re	Reynolds number, $\Omega R c_{ref}/\nu$
x,y,z,t	inertial coordinates
u,v,w	nondimensional inertial space velocities
u_B, v_B, w_B	u,v,w rotated from (x,y,z) directions to (ξ,η,ζ) directions

Presented at the American Helicopter Society Aeromechanics Specialists Conference, San Francisco, California, January 19-21, 1994.

δ	boundary layer thickness
δ^*	boundary layer displacement thickness
ν	kinematic viscosity at sea level, 1.5723×10^{-4} ft^2/s
ρ	density
ρ_∞	free stream density
θ	momentum thickness
Ω	rotor speed (381 rpm)
ξ,η,ζ,τ	blade-fixed computational coordinates

Introduction

Interest in the flow field of rotors in hover or axial flight has a long history. In particular, the demonstrated ability of highly-twisted rotors or propellers to delay stall and continue to generate lift under high thrust conditions has prompted numerous studies over the years. The ability of rotating, high incidence blade sections to maintain attached flow when non-rotating sections under similar conditions undergo flow separation has generated several explanations for this phenomenon, such as outward flow of the boundary layer, Coriolis effects, and rotor wake contraction.

One of the earliest experiments addressing the delayed-stall problem is Himmelskamp (Ref. 1). The Himmelskamp experiment investigated a two-bladed airscrew in axial flow in a duct. High section lift coefficients were attributed to the thinning of the boundary layer caused by the radial flow produced by the centrifugal force. Himmelskamp noted that the Coriolis force also contributes to keeping the flow attached at high angles of incidence. After the work of Ref. 1, several theoretical studies of laminar boundary layers on rotating flat plates emerged (Refs. 2 - 5). Harris (Ref. 6) summarized these theoretical efforts and also reviewed the experimental work completed through the mid-1960's in his study of radial flow effects on rotor blades.

At the time of Ref. 6, little or no work had been done on turbulent boundary layers on rotating blades. Tanner and Yaggy (Ref. 7) conducted an experimental investigation, using a chemical film technique, of the boundary layer on a UH-1 untwisted tail rotor blade in hover and compared results with non-rotating wind tunnel measurements. Reference 7 did not find any evidence of outward or radial flow of the boundary layer for the rotating case. Also, no apparent change in the boundary layer thickness was found when comparing rotating and nonrotating cases. However, Ref. 7 was not able to explore stalled conditions and suggested that outward flow of the boundary layer was still possible for regions of separated flow. McCroskey and Yaggy (Ref. 8) and Dwyer and McCroskey (Ref. 9) provided analyses for a laminar boundary layer on a rotating flat plate in forward flight, which led to the analysis of a turbulent boundary layer on a rotating flat plate by McCroskey, Nash, and Hicks (Ref. 10).

By the 1980's, literature from the wind turbine industry also began appearing on the subject of delayed stall, for example, Milborrow (Ref. 11) and Wood (Ref. 12). Also during this time period, hover tests of two full-scale tilt rotors (Refs. 13-14) and a 0.658-scale V-22 rotor (Ref. 15) were conducted. Narramore and Vermeland (Ref. 16) made one of the first attempts to address the delayed stall phenomenon using computational fluid dynamics (CFD) methods. Reference 16 performed calculations for the 0.658-scale rotor of Ref. 15, showing that the flow remained attached at inboard blade regions for very large collective angles while outboard regions experienced separated flow. No evidence of radial flow was found. However, the CFD analysis relied on a separate lifting-surface code to provide the wake induced angle-of-attack distribution at the blade. In addition, the grid spacing used near the blade surface was rather coarse. Tung and Branum (Ref. 17) conducted a hover test of a model tilt rotor with surface pressure measurements and compared these data with hover free wake codes coupled with a full-potential rotor code. The codes were unable to predict the pressure coefficient distributions for radial stations inboard of 50 percent. Tsung and Sankar (Ref. 18) investigated the effects of rotation on flow separation using CFD. However, the blade modeled was an untwisted blade with a BERP tip and results were only provided for the outer 35 percent of the blade. Calculations revealed that blade rotation allowed the flow to remain attached at incidence angles where separation occurred on a fixed wing. Most recently, Felker (Ref. 19) used five analytical models to predict tilt rotor hover performance and compared these predictions with the data from Refs. 13-15. In general, predicted power was greater than the measured power, especially at high thrusts. Several of the analyses relied on two-dimensional airfoil data for lift and drag, resulting in premature lift loss when the calculated angle of incidence at the blade section was beyond the two-dimensional stall angle.

Despite many studies investigating the delayed stall phenomenon, a complete and consistent explanation for this difficult problem does not exist. Accurately calculating a three-dimensional, rotating, turbulent boundary layer with areas of flow separation may not be possible for some time. Experimental measurements of the boundary layer under these conditions is also an intimidating task. The current CFD technology, however, does provide a means for scrutinizing the flow field details and may provide insight into the stall delay phenomenon.

The objective of this study is to shed light on the delayed stall phenomenon by examining the viscous flow field near the surface of a hovering rotor blade. Calculations are performed using a thin-layer Navier-Stokes CFD code. The paper will discuss the flow solver and solution, the grid geometry, the method of computing the boundary layer parameters, and the assumptions and approximations used in this study. The effect of blade twist and precone on the flow are presented. Two twist distributions, representative of a tilt rotor and of a conventional helicopter rotor blade, are used. Although precone has not been modeled in previous studies, precone does affect the velocities and centrifugal force seen by the blade. Thus, the precone effect is studied here. By examining the section force coefficients, regions of the blade are identified which warrant closer study. Then, the effect of blade twist on boundary layer parameters such as skin friction vectors and shape factor, in addition to surface pressure distributions are discussed. Velocity profiles for different chordwise and spanwise locations are also presented.

Description of Flow Solver and Solution

TURNS (Transonic Unsteady Rotor Navier-Stokes) is a versatile and robust Euler and Navier-Stokes CFD code developed by Srinivasan, et al (Refs. 20-23) at NASA Ames Research Center under U. S. Army Research Office support. This code has been used in many investigations of rotorcraft aerodynamic and acoustic phenomena, examples of which can be found in Refs. 20-23. Srinivasan, et al (Ref. 21) provides details of the finite difference scheme. A brief description of the governing equations and numerical scheme, taken from Ref. 23, is provided below. The governing equations are given by

$$\partial_\tau \hat{Q} + \partial_\xi \hat{E} + \partial_\eta \hat{F} + \partial_\zeta \hat{G} = \frac{1}{Re} \partial_\zeta \hat{S} \qquad (1)$$

where

$$Q = [\, \rho \;\; \rho u \;\; \rho v \;\; \rho w \;\; e \,]^T \;, \; \hat{Q} = Q/J \qquad (2)$$

$\hat{E}$, $\hat{F}$, $\hat{G}$ are the convective flux vectors and $\hat{S}$ is the viscous flux vector using the thin-layer approximation. The blade-fixed computational coordinates are defined by (ξ,η,ζ). The flux vectors have been normalized by the Jacobian J. The density, mass fluxes, and energy per unit volume are nondimensionalized by the far-field reference quantities. Re is the Reynolds number based on M_{tip} and a reference chord (defined as the chord at 0.75R for this investigation). The reference chord and sound speed are the characteristic length and velocity scales, respectively. The equation of state for a perfect gas and Eq. 1 describe the entire flow field. The numerical method uses a Roe upwind-biased scheme for all the coordinate directions with higher-order MUSCL-type limiting for the right-hand side. A lower-upper Gauss-Seidel implicit operator is used for the left-hand side. The governing equations are solved in the blade-fixed coordinate system, requiring a transformation that introduces source terms that account for the centrifugal force produced by blade rotation. The space metrics are evaluated using a finite volume formulation, while a finite difference formulation is used for the time metrics. The turbulence model in TURNS is the Baldwin-Lomax model.

The boundary conditions described in Refs. 22-23 are repeated here. At the blade surface, a no-slip condition is used with a finite velocity due to blade rotation. The surface pressure is obtained through the normal momentum equation and the density is evaluated by the adiabatic wall condition. In the azimuthal direction, a periodic flow condition is used, hence the need to only model one blade. At the blade root plane, the inertial velocity components are obtained by assuming the velocity gradient in the spanwise direction is zero at the root. This boundary condition can affect the development of the root vortex and requires improvement. To prevent flow recirculation in the computational domain, the far-field flow is determined by superimposing the flow from a three-dimensional sink (placed at the center of rotation) and momentum theory. Srinivasan, et al (Ref. 23) provides expressions for the velocity entering the computational domain at the upper and side boundaries and the exit velocity at the lower boundary. Since total performance predictions are not the objective of this study, the far-field boundary conditions are considered adequate.

The solution is provided by TURNS in terms of Q at every grid point. For this study, Q, the (x,y,z) grid, and the metrics at each grid point calculated by TURNS are then used by a separate program to compute the skin friction and inertial velocities (rotated from the (x,y,z) directions to the (ξ,η,ζ) directions), the boundary layer shape factor, and surface pressure coefficients.

Description of Grid

The finite-difference grid is of C-H topology, with C in the wrap-around direction and H in the spanwise direction. The grid dimensions are 181 points in the wrap-around direction, with 49 points in the spanwise and normal directions. The outer boundary is one rotor diameter above and below the rotor plane. Only one blade is modeled. The distance to the first point off the blade surface in the normal direction is $0.00004c_{ref}$ which is approximately 0.27% of the boundary layer thickness at the 0.75 radial station. The grid stretching in the normal

direction gives 15-20 grid points in the boundary layer. The spanwise location of the outer boundary is one rotor radius beyond the blade tip. Figure 1a and 1b show the computational coordinate system and a plan view of the grid geometry, resepctively. The inner boundary is at the blade root (0.23 radial station) and the reference chord is located at the 0.75 radial station.

For this investigation, the grid generator was modified to incorporate twist distributions typical of tilt rotor blades and conventional rotor blades. In addition, the option of blade precone was included. The airfoils used are similar to those developed at Bell Helicopter Textron. Inc.; all blade geometries incorporated the same spanwise distribution of airfoils. Figure 2a and 2b show the two twist distributions studied in this paper, without and with the collective pitch, respectively. The collective pitch is 16 deg for the high twist case and 19 deg for the low twist case. Different collectives were required in order to match rotor thrust coefficients. The high twist is representative of a tilt rotor blade and is defined as the baseline case for this study. Figure 3 shows spanwise cuts at the blade root for the two twist distributions. The collective pitch is included in the geometry. In Fig. 3a, the severe twist and a requirement by the grid generator to enforce a zero-slope at the outer boundary cause a kink in the grid aft of the trailing edge. The grid is designed to capture the flow at the blade surface, but is not optimized to capture tip vortex formation, the trailed wake behind the blade, or the wake underneath the blade from the preceding blades. Since performance is not the focus of this investigation, the grid is considered sufficient for analyzing the flow on and very near the blade surface. Applications such as Ref. 23 imply that the boundary conditions and grid are adequate to define the aerodynamic environment near the blade.

Definition of Rotation Matrices

In order to calculate skin friction vectors and shape factor values on the blade surface, the inertial space velocities and the stress tensor must be rotated to the (ξ,η,ζ) directions. Orthogonal metrics x_ξ, ξ_x, etc., can be used to form rotation matrices for this transformation. However, because the grid is only nominally orthogonal at the blade surface for the geometries in this study, the rotation matrices defined by the metrics will not be orthogonal matrices. Therefore, rotation matrices are developed directly from the surface geometry. This is done by first constructing a vector t_ξ tangent to the ξ-direction at the blade surface for a (j,k) point, then making t_ξ into a unit vector, u_ξ. Next, a vector ε_η tangent to the η-direction is used to construct a vector t_η orthogonal to u_ξ. The vector t_η is then made into a unit vector u_η. The third orthogonal vector, u_ζ, is obtained by taking the cross product between u_ξ and u_η. Finally, the rotation matrices C_{BA} and C_{AB} (between inertial space A and the blade surface B) are constructed. The procedure is shown in the following equations.

$$t_\xi = \begin{bmatrix} 0.5\,(x_{j+1,k,1} - x_{j-1,k,1}) \\ 0.5\,(y_{j+1,k,1} - y_{j-1,k,1}) \\ 0.5\,(z_{j+1,k,1} - z_{j-1,k,1}) \end{bmatrix} \tag{3}$$

$$\varepsilon_\eta = \begin{bmatrix} 0.5\,(x_{j,k+1,1} - x_{j,k-1,1}) \\ 0.5\,(y_{j,k+1,1} - y_{j,k-1,1}) \\ 0.5\,(z_{j,k+1,1} - z_{j,k-1,1}) \end{bmatrix} \tag{4}$$

$$t_\eta = ([I] - u_\xi\, u_\xi^T)\, \varepsilon_\eta \tag{5}$$

$$u_\xi = \frac{t_\xi}{|t_\xi|},\quad u_\eta = \frac{t_\eta}{|t_\eta|},\quad u_\zeta = u_\xi \times u_\eta \tag{6}$$

$$[C_{BA}] = \begin{bmatrix} u_\xi^T \\ u_\eta^T \\ u_\zeta^T \end{bmatrix} \tag{7}$$

$$[C_{AB}] = [\, u_\xi \quad u_\eta \quad u_\zeta \,] \tag{8}$$

The rotation matrices are defined at the blade surface (ℓ=1) for a particular (j,k) location and then used for all ℓ at that location. The velocities and stress tensor are then transformed by

$$\begin{bmatrix} u_B \\ v_B \\ w_B \end{bmatrix} = [C_{BA}] \begin{bmatrix} u \\ v \\ w \end{bmatrix} \tag{9}$$

$$\begin{bmatrix} \tau_{\xi\xi} & \tau_{\xi\eta} & \tau_{\xi\zeta} \\ \tau_{\eta\xi} & \tau_{\eta\eta} & \tau_{\eta\zeta} \\ \tau_{\zeta\xi} & \tau_{\zeta\eta} & \tau_{\zeta\zeta} \end{bmatrix} = [C_{BA}] \begin{bmatrix} \tau_{xx} & \tau_{xy} & \tau_{xz} \\ \tau_{yx} & \tau_{yy} & \tau_{yz} \\ \tau_{zx} & \tau_{zy} & \tau_{zz} \end{bmatrix} [C_{AB}] \tag{10}$$

Although TURNS assumes a thin viscous layer near the blade surface to compute Q, the complete expressions for the tensor elements in the (x,y,z) system (Eq. 10) were evaluated before being transformed.

Determining Boundary Layer Parameters

The following equations from White (Ref. 24) were used to calculate the displacement thickness, momentum thickness, and shape factor of the boundary layer at each (j,k) location on the blade upper surface.

$$\delta^* = \int_0^{\infty} \left(1 - \frac{\rho}{\rho_e} \frac{u}{U_e} \right) dz = \sum_{\ell=1}^{\ell_e} \left(1 - \frac{\rho_\ell}{\rho_{\ell e}} \frac{u_\ell}{U_{\ell e}} \right) \Delta\ell \qquad (11)$$

$$\theta = \int_0^{\infty} \frac{\rho}{\rho_e} \frac{u}{U_e} \left(1 - \frac{u}{U_e} \right) dz = \sum_{\ell=1}^{\ell_e} \left(\frac{\rho_\ell}{\rho_{\ell e}} \frac{u_\ell}{U_{\ell e}} \right) \left(1 - \frac{u_\ell}{U_{\ell e}} \right) \Delta\ell \qquad (12)$$

$$H = \frac{\delta^*}{\theta} \qquad (13)$$

$$\Delta\ell = \left[(x_{\ell+1} - x_\ell)^2 + (y_{\ell+1} - y_\ell)^2 + (z_{\ell+1} - z_\ell)^2 \right]^{0.5} \qquad (14)$$

$$U_{\ell e} = \left[(u_{B\ell e} - u_{B1})^2 + (v_{B\ell e} - v_{B1})^2 \right]^{0.5} \qquad (15)$$

Since a definition does not exist for the boundary layer edge of a rotating twisted blade, an approximation using a flat plate analogy is used. The edge of the boundary layer was first estimated by calculating the boundary layer thickness, δ, for turbulent flow over a flat plate using the Reynolds number at the 0.75 radial station. Next, the ℓ-value (ℓmax) corresponding to a distance δ away from the blade surface was determined for the 0.75 radial station and used as an upper limit on ℓe (the ℓ-value defining the boundary layer edge). The boundary layer thickness will vary for different (j,k) locations on the surface; therefore, ℓe was determined by searching for the maximum velocity magnitude from ℓ=1 to ℓ=ℓmax at each (j,k) location. This maximum velocity was then defined as $U_{\ell e}$ and the corresponding ℓ-value defined as ℓe. The dot product of the edge velocity vector and the velocity vectors from ℓ=1 to ℓ=ℓe was then computed to obtain the components u_ℓ in the direction of the edge velocity, as shown in the equation below (note that the velocity, u_ℓ, is zero at ℓ=1):

$$u_\ell = \frac{(u_{B\ell} - u_{B1})(u_{B\ell e} - u_{B1}) + (v_{B\ell} - v_{B1})(v_{B\ell e} - v_{B1})}{U_{\ell e}} \qquad (16)$$

Finally, δ^*, θ, and H were computed.

The skin friction values in the ξ- and η-directions are computed using the following:

$$Cf_{\xi\zeta} = \tau_{\xi\zeta}/(0.5\rho_\infty(\Omega r)^2) \qquad (17)$$

$$Cf_{\eta\zeta} = \tau_{\eta\zeta}/(0.5\rho_\infty(\Omega r)^2) \qquad (18)$$

Results

The effects of blade twist and precone on section force coefficients and flow parameters are studied by performing calculations for three blade geometries: tilt rotor blade twist distribution (baseline case), 10 deg linear twist distribution (low twist case, simulating a helicopter case), and tilt rotor blade twist distribution with 2 deg precone. Figure 2 shows the baseline and low twist distributions used for the calculations. All three geometries incorporate the same spanwise airfoil distribution and chord distribution (chord distribution shown in Fig. 4). For the three cases, Mtip = 0.68, Reynolds number based on Mtip and the reference chord = 10.1 million, and CT=0.017 (nominally). The collective pitch for the baseline twist cases is 16 deg; the low twist case collective is 19 deg (Fig. 2b). Table 1 provides a summary of the rotor parameters and operating conditions for the calculations presented.

Residual and Rotor Thrust Coefficient Behavior

TURNS was run for 7000 iterations for each of the three cases. Figure 5 shows the residual behavior. The residual for iterations less than 1000 were computed using a grid coarsened by using every other grid point in all three directions. In Fig. 5, RSUM (L2 norm) represents the residual over the entire grid volume. Less than two orders drop in magnitude of the L2 norm is shown in the first 2000 iterations for all three cases. Since the largest contributor to the L2 norm was usually located at the outer boundary, a residual within the grid volume of interest was computed. RSUMX represents the residual over a volume defined by the blade surface from the root to 0.96 radial station and out to 30 grid points away from the surface (a distance of approximately 0.10-0.15 of the reference chord). RSUMX shows several orders of magnitude drop in the first 2000 iterations.

The rotor CT behavior is shown in Fig. 6. The oscillations are possibly caused by the movement of the near field tip vortex trajectory. These oscillations are more severe if the grid near the tip becomes coarser. The CT value averaged from 2000 to 7000 iterations is nominally 0.017 for all three cases.

Sectional Force Coefficients

Examination of the spanwise behavior of the sectional forces is instructive for identifying flow regions of interest on the blade. Figure 7a and 7b present the section thrust (Ct) and in-plane (Cx) force coefficients, respectively. Figure 7a shows that the overall thrust produced by all three cases is nominally the same. The baseline twist case (with and without precone), however, produces more thrust for radial stations less than 0.6 compared to the low twist case. Outboard of 0.85 radial station, the thrust is nearly the same for both twist cases, even though the low twist case has a larger blade pitch in this region (Fig. 2b). Figure 7b shows that the Cx distribution is markedly different between the two twist cases, especially outboard of the 0.6 radial station. Since Cx times the blade radial station integrates to the rotor torque, the differences in Cx between the two twist cases at the outboard region is more important than the differences at the inboard region when computing rotor performance. The higher Cx near the blade tip for the low twist case implies a performance worse than the baseline twist case, which is consistent with previous tilt rotor measurements. The low twist case has a higher geometric pitch than the baseline case outboard of 0.6 radial station which will contribute to a higher induced drag. However, the magnitude of the wake effect compared to the increase in profile drag is unknown.

The behavior of the blade normal (Cn) force coefficient based on the local chord and radial station is also revealing (Fig. 8). Cn is normal to the local blade chord. The baseline twist blade sections generate more normal force than the low twist blade for radial stations less than 0.6. The Cn begins decreasing at 0.8 radial station for the low twist blade; this drop-off in Cn is delayed until approximately 0.85 for the baseline twist blades. If Cn is assumed to be approximately the lift coefficient, some comparisons can be made with two-dimensional measurements. For example, the maximum 2D lift coefficient for the airfoils used between 0.2 and 0.45 radial stations is 1.2-1.3. Clearly, Fig. 8 shows the baseline twist cases exceed this value, while the low twist case does not. This behavior is similar to that seen in other studies in the literature (Refs. 17 and 19). From 0.4 to 0.85 radial station, however, both twist distributions give Cn values below the maximum 2D lift coefficient.

Since the above results indicate the blade outboard region has a larger impact on performance than the inboard region, as indicated by the dramatic differences in Cx in Fig. 7b, a closer look at the blade region outboard of 0.6 radial station is warranted.

Skin Friction

Figures 9-11 show skin friction vectors on the blade upper surface outboard of 0.789 radial station for the baseline twist, low twist, and baseline twist with precone, respectively. For clarity, every other chordwise grid point is shown. For radial stations inboard of 0.789, the skin friction vectors are essentially chordwise for all three cases without any flow separation. There is a dramatic difference between the baseline and low twist cases (compare Figs. 9 and 10). The low twist case shows a significant amount of outward spanwise flow, starting from the 0.789 radial station. The baseline twist case shows the flow is chordwise out to 0.836 radial station. The 0.789 and 0.836 radial locations correspond to the approximate spanwise locations where Cn (Fig. 8) begins to decrease for the low and baseline twist cases, respectively. The addition of 2 deg of precone to the baseline twist does not have a significant effect (compare Figs. 9 and 11). Both twist cases appear to have a counterclockwise flow pattern over a portion of the blade: between 0.857 and 0.908 radial stations for the baseline twist and between 0.789 and 0.892 radial stations for the low twist case. The velocity vectors (with components u_B-$u_{B\ell=1}$ and $v_{B\ell}$ $v_{B\ell=1}$) at approximately 0.01 chord distance above the blade are shown in Figs. 12 and 13 for the baseline and low twist cases, respectively. The velocity vectors indicate there is some spanwise flow near the blade surface and also some regions of swirl; the velocity vectors are consistent with the skin friction vectors.

Velocity Profiles

Velocity profiles in the boundary layer are examined for several chordwise stations at the 0.857 radial station for the baseline and low twist case in Figs. 14 and 15, respectively. The chordwise, spanwise, and normal velocity components are u_B-$u_{B\ell=1}$, $v_{B\ell}$-$v_{B\ell=1}$, and $w_{B\ell}$-$w_{B\ell=1}$, respectively. In Fig. 14, the flow remains attached over the blade chord. There is a small contribution from the spanwise component; the normal component is essentially zero. For the low twist case, Fig. 15 indicates that the flow is already separated close to the leading edge, after which the chordwise velocity becomes increasingly negative (reverse flow). The spanwise velocity grows in magnitude as the trailing edge is approached until the flow is almost entirely spanwise, which is consistent with Figs. 10 and 13.

Pressure Coefficient Profiles

The surface pressure coefficient (Cp) distributions cor responding to the radial station (0.857) of Figs. 14 and 15 is shown in Fig. 16. The baseline case with precone has nearly the same Cp distribution as the baseline case without precone. In Fig. 16, the lower surface Cp distributions are essentially the same. On the upper surface, the low twist case has a severe adverse pressure gradient starting from the leading edge and thereafter remains relatively constant until the trailing edge. This behavior indicates separated flow (seen in Fig. 15) over most of the upper surface. The difference in the upper surface Cp distribution contributes to the difference in Cx at this radial station (Fig. 7b).

Shape Factor

The shape factor is a useful parameter for identifying separation points for two-dimensional boundary layers. For turbulent flat plate flow, the shape factor is on the order of 1.2 (Ref. 24), with separation occurring near H=2 (Schlicting, (Ref. 25)). Computing shape factors for three-dimensional, rotating blades at large incidence angles using Eqs. 11-13 may be inappropriate, especially using the approximate method for finding the boundary layer edge. The intent here, however, is to ascertain whether the behavior of H, not necessarily the value of H, can serve as another indicator of the flow behavior. Figure 17 presents chordwise shape factor distributions for several spanwise stations for both the baseline and low twist cases. Comparing Fig. 17 with the skin friction plots reveals the chordwise location where H undergoes a sign change gives an indication of the change in direction of the skin friction vectors (from outward spanwise to inward spanwise). The sign change also reflects the reversal in sign of U_{ℓ_e}, the velocity at the boundary layer edge.

Concluding Remarks

The objective of this study was to shed light on the delayed stall phenomenon by examining the viscous flow field near the surface of a hovering rotor blade. The Navier-Stokes CFD code TURNS was used to perform calculations for three blade geometries which included a tilt rotor blade twist distribution (baseline), conventional helicopter rotor blade twist distribution, and the baseline twist distribution with 2 deg of precone. Calculations were performed for thrust conditions near stall. Although the rotor thrust coefficient was nominally the same for the cases using the two twist distributions, large differences were found in the section in-plane and normal force coefficients. These results imply that the blade outboard region, rather than the inboard region, may provide the majority of the performance advantage of the baseline case over the low twist case. Skin friction, velocities near the blade, and surface pressures for the two twist distributions reveal significant differences in the blade outboard region.

This investigation was entirely computational. Given the assumptions of this study, the following observations are made:

1. The in-plane force coefficient is much higher outboard of 0.6 radial station for the low twist case compared to the baseline twist case. This implies a performance penalty for the low twist case.

2. The normal force coefficient is much higher inboard of 0.6 radial station for the baseline twist case compared to the low twist case.

3. For radial stations outboard of 0.789, there is more outward spanwise flow on the blade upper surface for the low twist case than for the baseline twist case. There is evidence of swirling flow near the blade surface for both twist cases.

4. For radial stations inboard of 0.789 radial stations, the upper surface flow remains attached and chordwise in direction for both the baseline and low twist cases.

5. The sign change in shape factor provides an indication of spanwise flow direction.

6. Adding 2 deg of precone to the baseline twist distribution has no significant effect on the blade flow field.

Additional work is needed to elucidate the fluid dynamic mechanisms involved in the observed flows. Before the above observations can be considered conclusive, the following actions are required: improve boundary condition at the blade root, smooth kinks in the grid caused by high twist, increase grid density, investigate the role of the tip vortex and wake on stall behavior, investigate alternate turbulence model, and determine an equivalent three-dimensional shape factor.

Acknowledgements

The authors thank Dr. J. D. Baeder (formerly of the U. S. Army AFDD at NASA Ames) of the University of Maryland for providing the grid generation code and for discussions regarding the use of the TURNS code. Also, the helpful discussions with Dr. G. R. Srinivasan of JAI Associates, Inc. and Prof. J. R. Spreiter of Stanford University are gratefully acknowledged. Finally, the authors thank Dr. F. F. Felker, III for suggesting that this particular research topic be studied using a Navier-Stokes code.

References

1. Himmelskamp, H., "Profile Investigations of a Rotating Airscrew," Reports of the Max-Planck-Institut fur Stromungsforschung, Gottengen, No.2, 1950.

2. Fogarty, L. E., "The Laminar Boundary Layer on a Rotating Blade," *Journal of the Aeronautical Sciences*, Vol. 18, (4), April 1951.

3. Tan, H. S., "On Laminar Boundary Layer over a Rotating Blade," *Journal of the Aeronautical Sciences*, Vol. 20, (11), November 1953.

4. Rott, N. and Smith, W. E., "Some Examples of Laminar Boundary-Layer Flow on Rotating Blades," *Journal of the Aeronautical Sciences*, Vol. 23, (11), November 1956.

5. Banks, W. H. and Gadd, G. E., "Delaying Effect of Rotation on Laminar Separation," *AIAA Journal*, Vol. 1, (4), April 1963.

6. Harris, F. D., "Preliminary Study of Radial Flow Effects on Rotor Blades,"*Journal of the American Helicopter Society*, Vol. 11, (3), 1966.

7. Tanner, W. H. and Yaggy, P. F., "Experimental Boundary Layer Study on Hovering Rotors," *Journal of the American Helicopter Society*, Vol. 11, (3), 1966.

8. McCroskey, W. J. and Yaggy, P. F., "Laminar Boundary Layers on Helicopter Rotors in Forward Flight," *AIAA Journal*, Vol. 6, (10), October 1968.

9. Dwyer, H. A., and McCroskey, W. J., "Crossflow and Unsteady Boundary-Layer Effects on Rotating Blades," AIAA Paper No. 70-50, AIAA 8th Aerospace Sciences Meeting, New York, NY, January 1970.

10. McCroskey, W. J., Nash, J. F., and Hicks, J. G., "Turbulent Boundary-Layer Flow over a Rotating Flat-Plate Blade," *AIAA Journal* , Vol. 9, (1), January 1971.

11. Milborrow, D. J., "Changes in aerofoil characteristics due to radial flow on rotating blades," 7th British Wind Energy Association Conference, Oxford, England, March 1985.

12. Wood, D. H., "Some Effects of Finite Solidity on the Aerodynamics of Horizontal Axis Wind Turbines," *Journal of Wind Engineering and Industrial Aerodynamics*, Vol. 26, 1987.

13. Felker, F. F., Betzina, M. D., and Signor, D. B., "Performance and Loads Data from a Hover Test of a Full-Scale XV-15 Rotor," NASA TM 86833, November 1985.

14. Felker, F. F., Young, L. A., and Signor, D. B., "Performance and Loads Data from a Hover Test of a Full-Scale Advanced Technology XV-15 Rotor," NASA TM 86854, January 1986.

15. Felker, F. F., Signor, D. B., Young, L. A., and Betzina, M. D., "Performance and Loads Data from a Hover Test of 0.658-Scale V-22 Rotor and Wing," NASA TM 89419, April 1987.

16. Narramore, J. C. and Vermeland, R., "Use of Navier-Stokes Code to Predict Flow Phenomena Near Stall as Measured on a 0.658-Scale V-22 Tiltrotor Blade," AIAA Paper No. 89-1814, AIAA 20th Fluid Dynamics, Plasma Dynamics, and Lasers Conference, Buffalo, NY, June 1989.

17. Tung, C. and Branum, L.,"Model Tilt-Rotor Hover Performance and Surface Pressure Measurement," 46th Annual National Forum of the American Helicopter Society, Washington, D. C., May 1990.

18. Tsung, F. and Sankar, L. N., "Numerical Simulation of Flow Separation for Rotors and Fixed Wings," AIAA Paper No. 92-0635, AIAA 30th Aerospace Sciences Meeting, Reno, NV, January 1992.

19. Felker, F. F., "Accuracy of Tilt Rotor Hover Performance Predictions," NASA TM 104023, June 1993.

20. Srinivasan, G. R. and Baeder, J. D., "Recent Advances in Euler and Navier-Stokes Methods for Calculating Helicopter Rotor Aerodynamics and Acoustics," 4th International Symposium on Computational Fluid Dynamics, Davis, CA, September 1991.

21. Srinivasan, G. R. and Baeder, J. D., "TURNS: A Free-Wake Euler and Navier-Stokes Numerical Method for Helicopter Rotors," *AIAA Journal*, Vol. 31, (5), May 1993.

22. Srinivasan, G. R., Baeder, J. D., Obayashi, S., and McCroskey, W. J., "Flowfield of a Lifting Rotor in Hover - A Navier-Stokes Simulation," *AIAA Journal*, Vol. 30, (10), October 1992.

23. Srinivasan, G. R., Raghavan, Duque, E. P. N., and Mc Croskey, W. J., "Flowfield Analysis of Modern Helicopter Rotors in Hover by Navier-Stokes Method," *Journal of the American Helicopter Society*, Vol. 38, (3), July 1993.

24. White, F. M., *Viscous Fluid Flow*, McGraw-Hill, Inc., 1974, p. 494, 606.

25. Schlicting, H. S., *Boundary-Layer Theory*, McGraw-Hill, Inc., 1968, pp. 636-643.

Table 1. Rotor parameters and operating conditions

blade radius	19 ft
chord at 0.75 radial station	25.075 in
root cutout (r/R)	0.231
solidity	0.105
rotor speed	381 rpm
Mtip	0.68
Reynolds number (based on tip speed and c_{ref})	10.1×10^6
collective pitch at 0.75R (baseline twist, precone=0 deg)	16 deg
collective pitch at 0.75R (low twist, precone=0 deg)	19 deg
collective pitch at 0.75R (baseline twist, precone=2 deg)	16 deg
C_T (baseline twist, precone= 0 deg) at 7000th iteration	0.0176
C_T (low twist, precone= 0 deg) at 7000th iteration	0.0171
C_T (baseline twist, precone= 2 deg) at 7000th iteration	0.0177

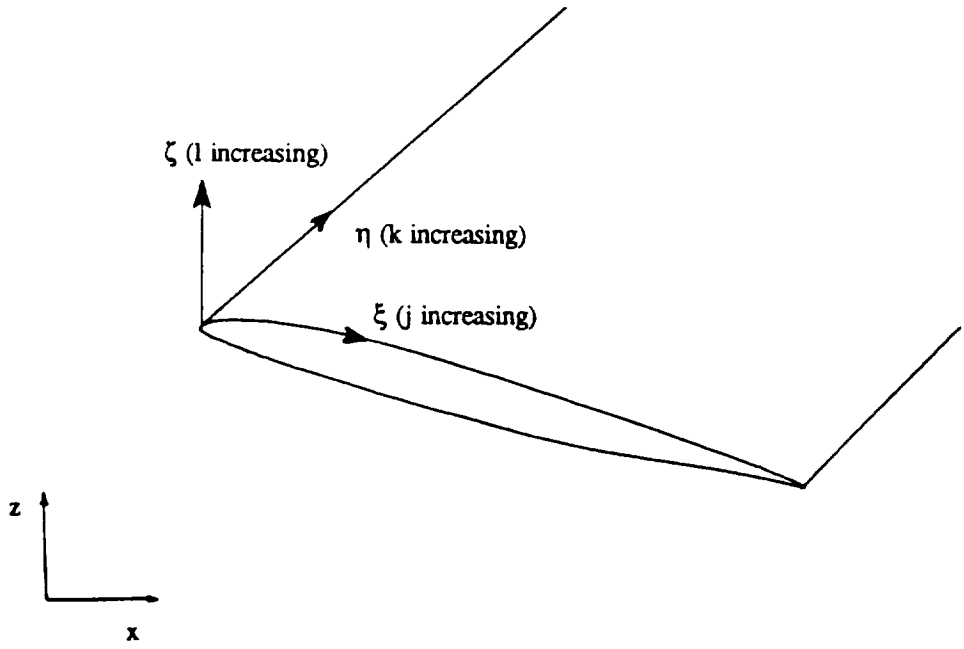

(a)

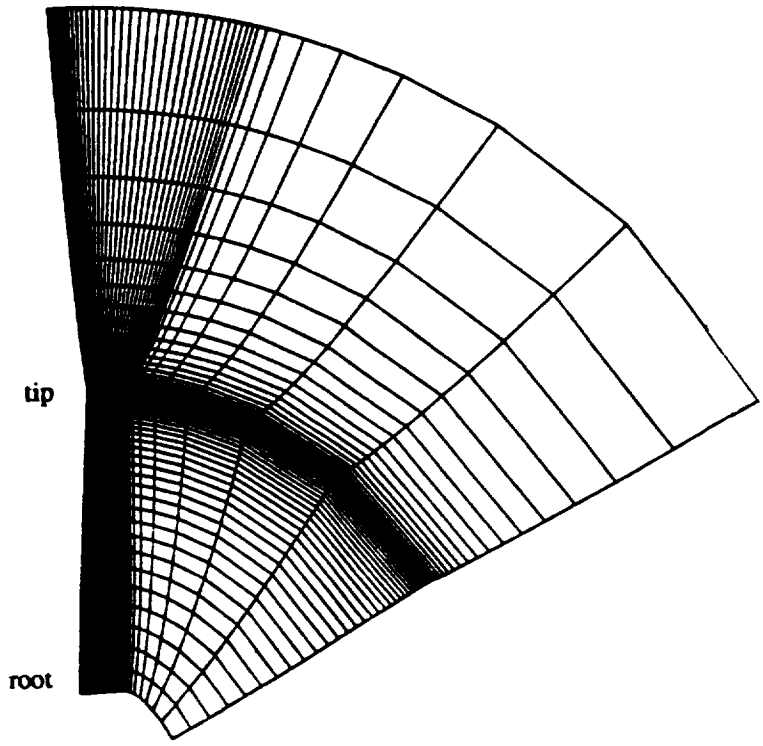

(b)

Figure 1. Grid geometry. (a) coordinate system, (b) planview of ℓ=1 surface (every other grid point shown)

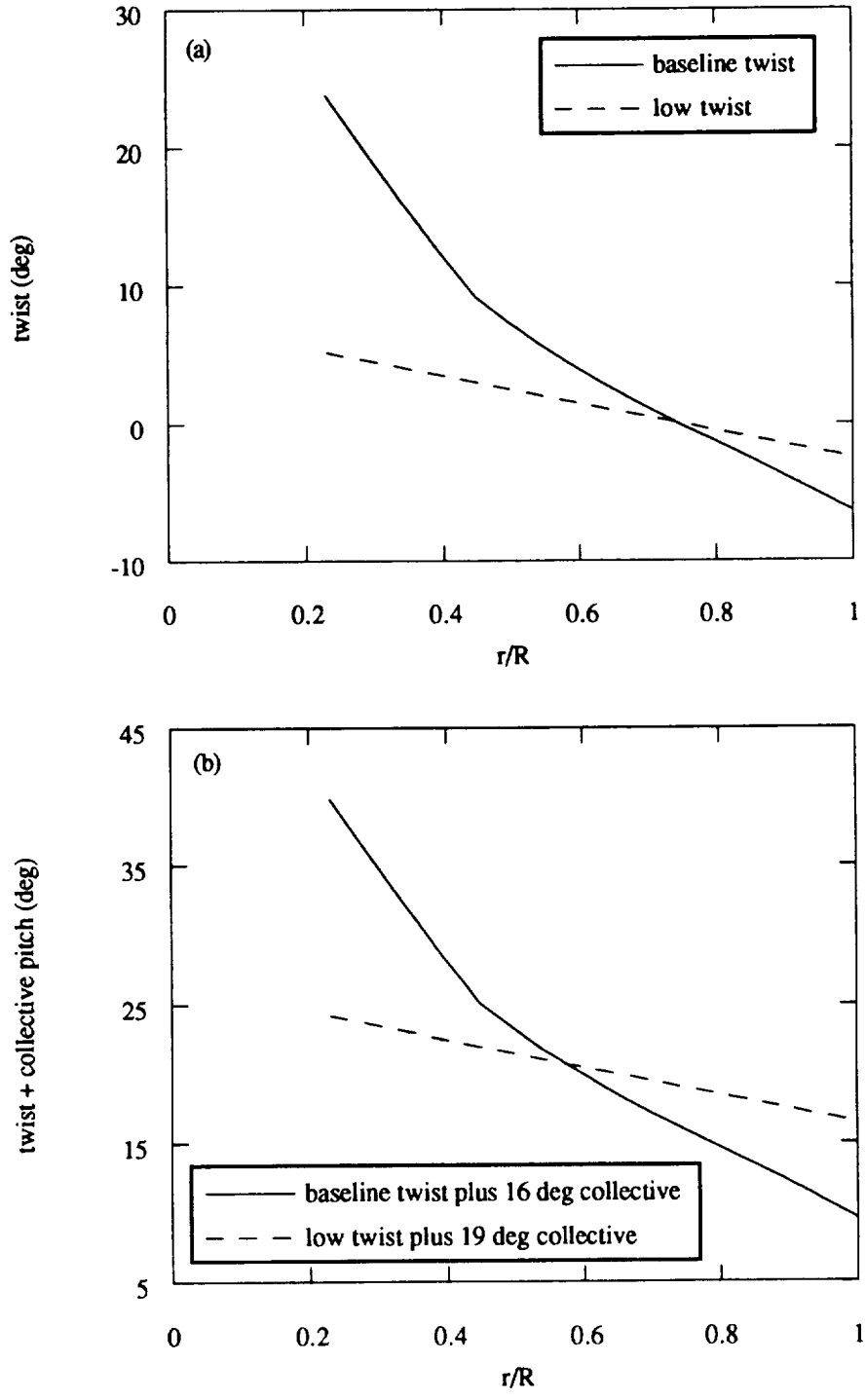

Figure 2. Built-in twist distributions. (a) without collective pitch (b) with collective pitch

(a)

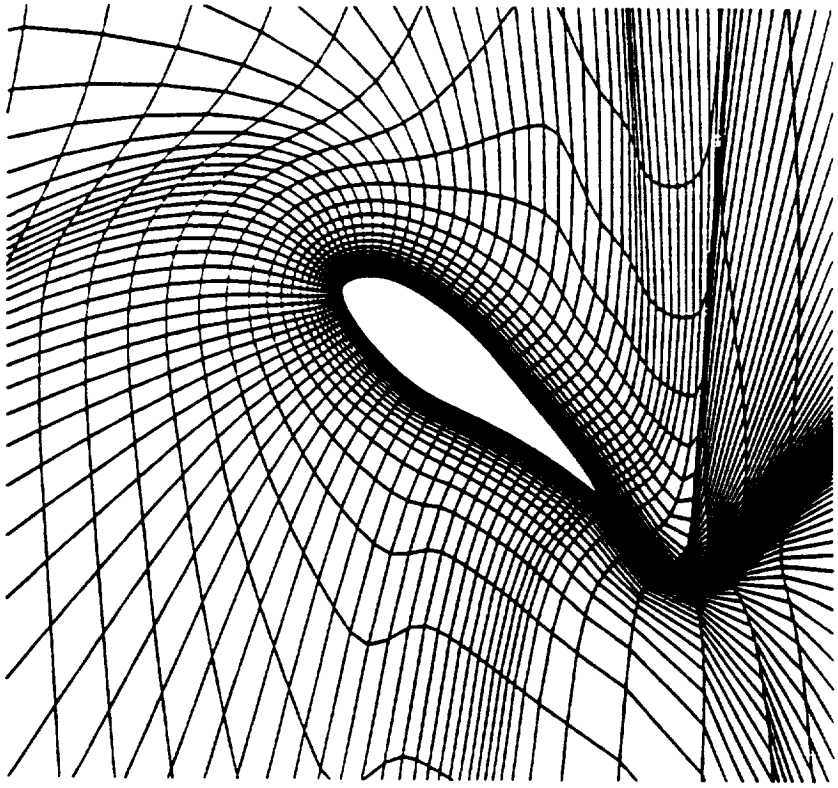

(b)

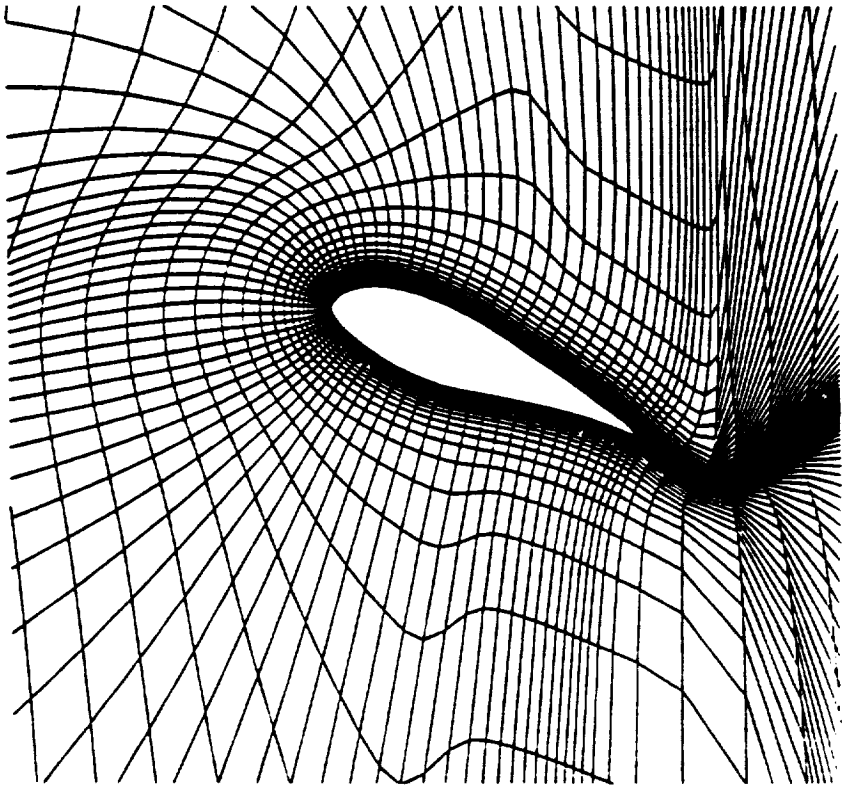

Figure 3. Grid geometry at blade root (every other chordwise grid point shown). (a) baseline twist, precone=o deg, (b) low twist, precone=0 deg

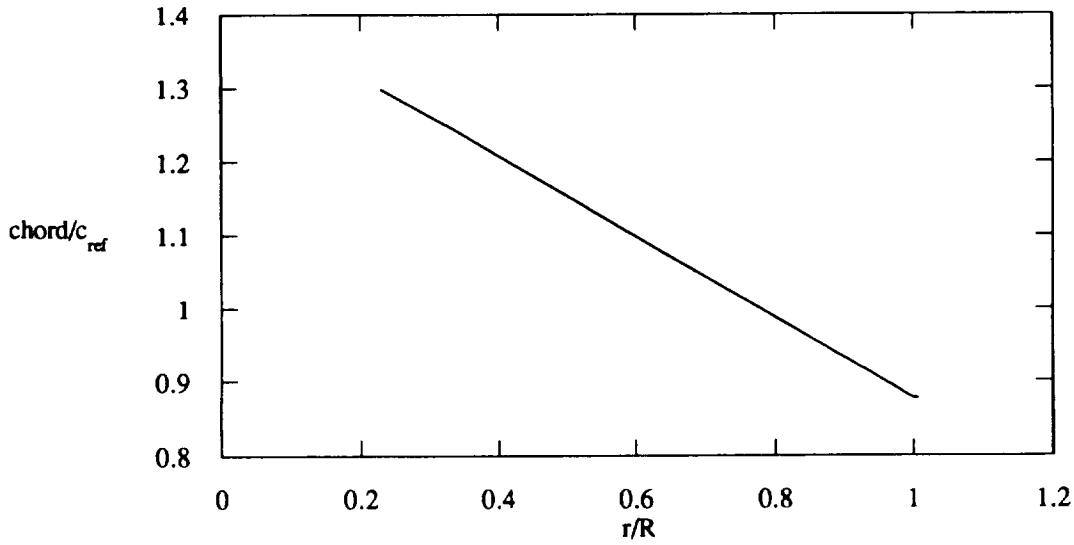

Figure 4. Spanwise chord variation.

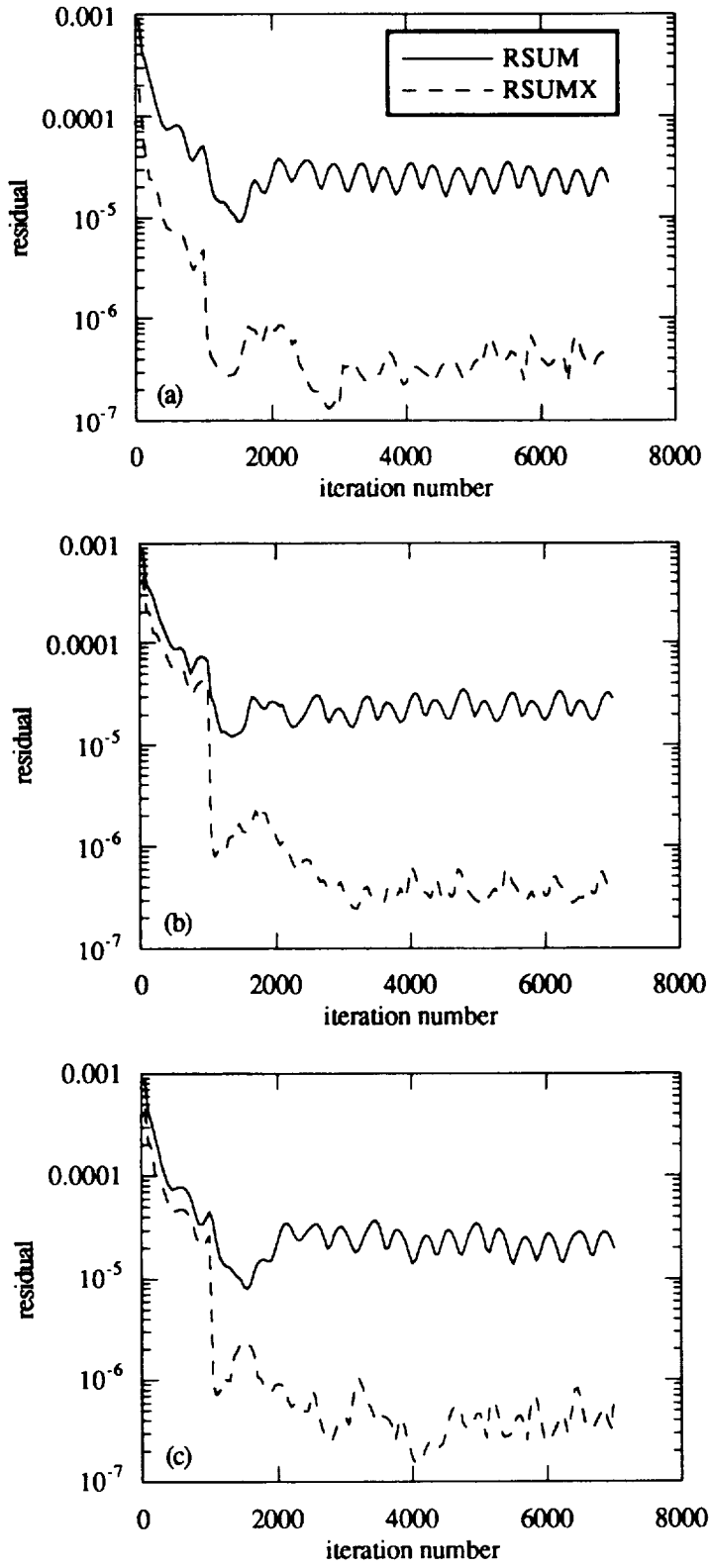

Figure 5. Residual behavior. a) baseline twist, precone=0 deg, b) low twist, precone=0 deg, c) baseline twist, precone=2 deg

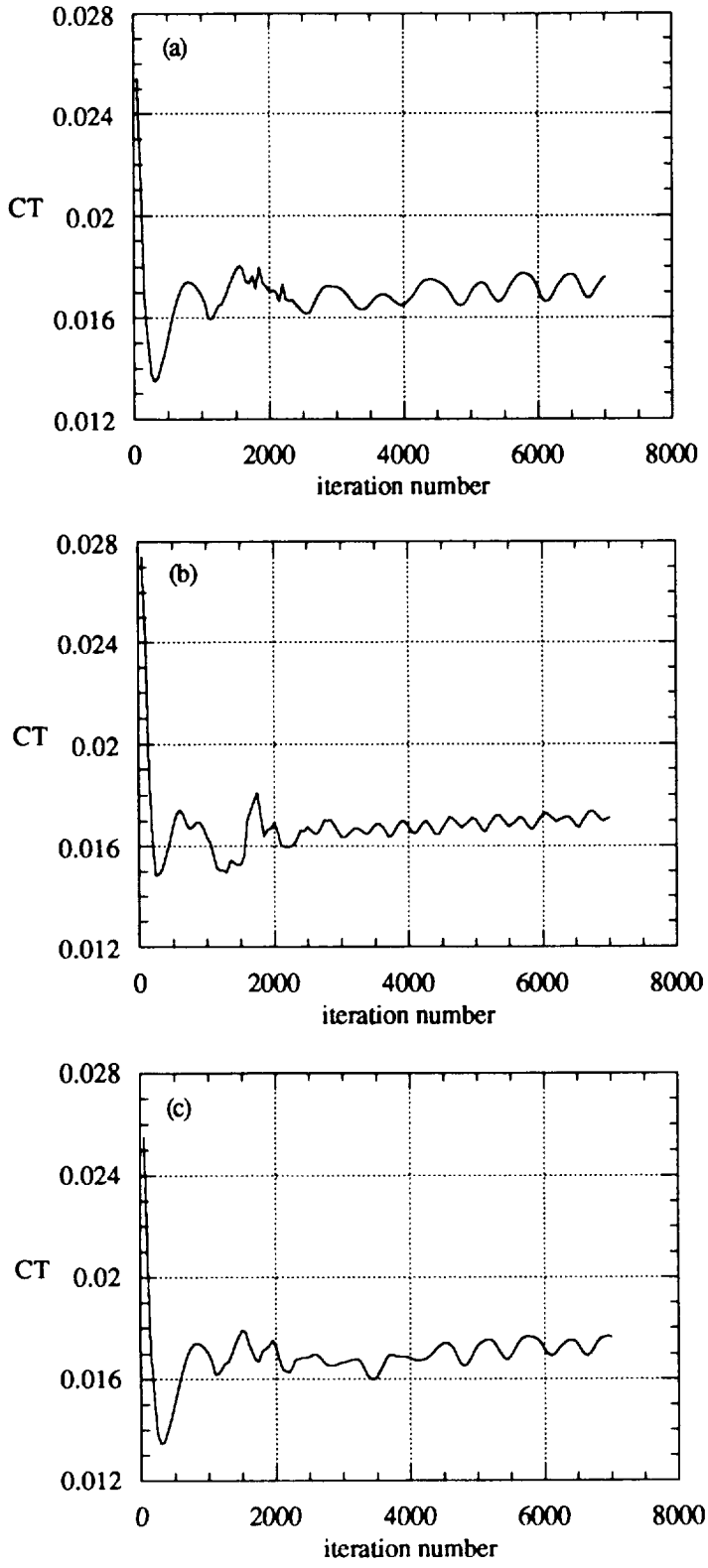

Figure 6. CT behavior. a) baseline twist, precone=0 deg, b) low twist, precone=0 deg, c) baseline twist, precone=2 deg

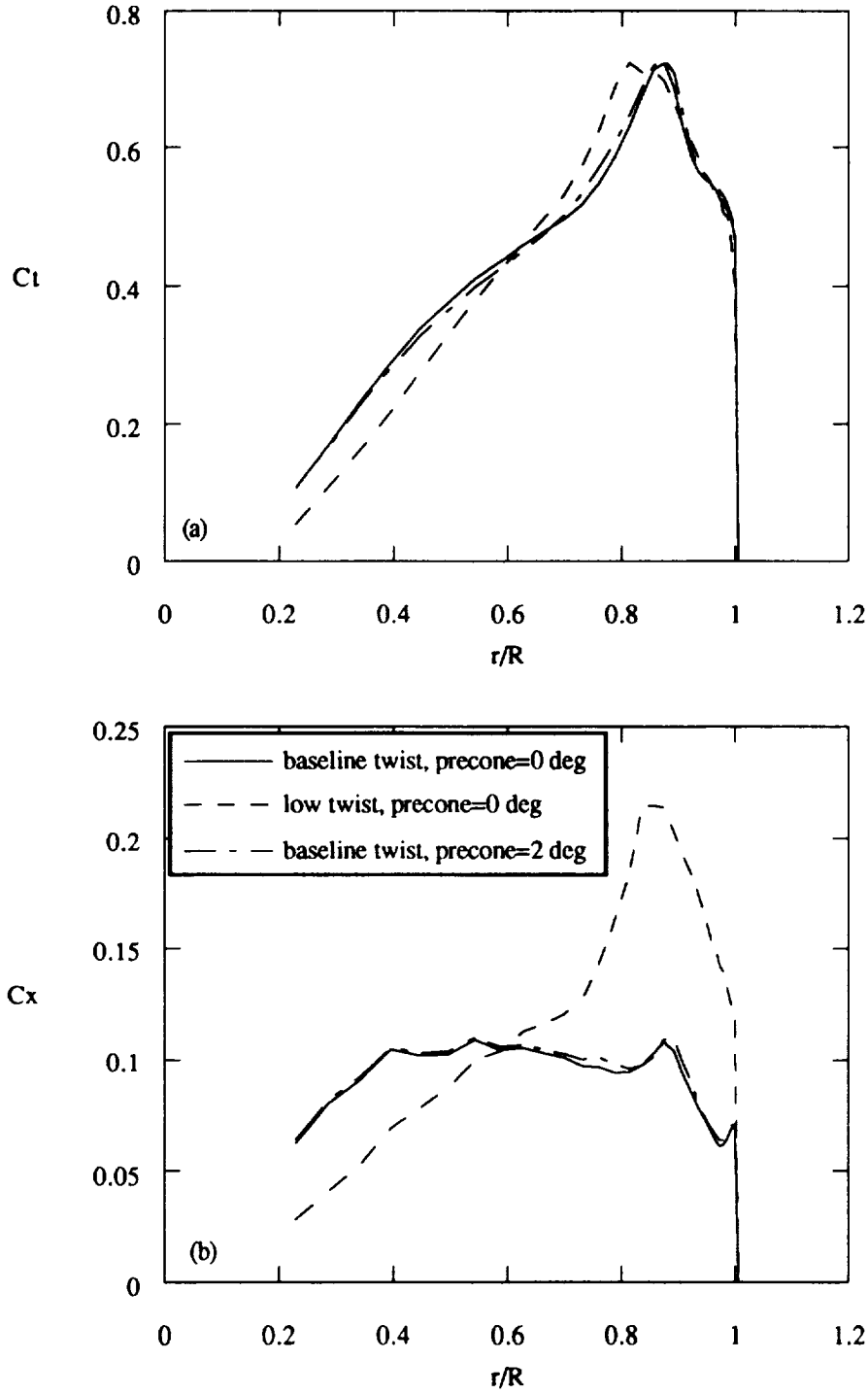

Figure 7. Spanwise variation of thrust and in-plane force coefficient. (a) thrust coefficient, (b) in-plane force coefficient

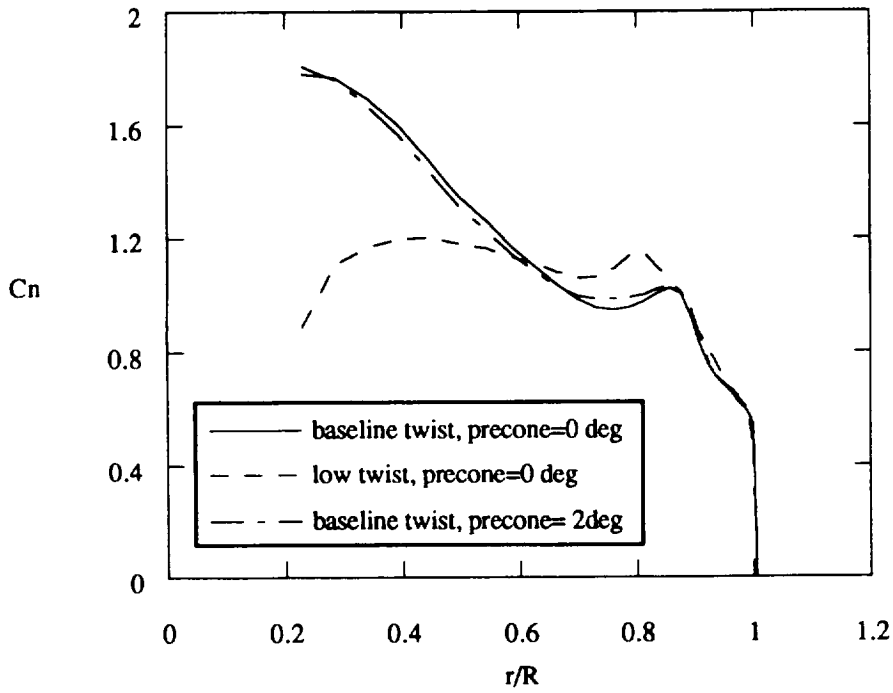

Figure 8. Spanwise variation of normal force coefficients.

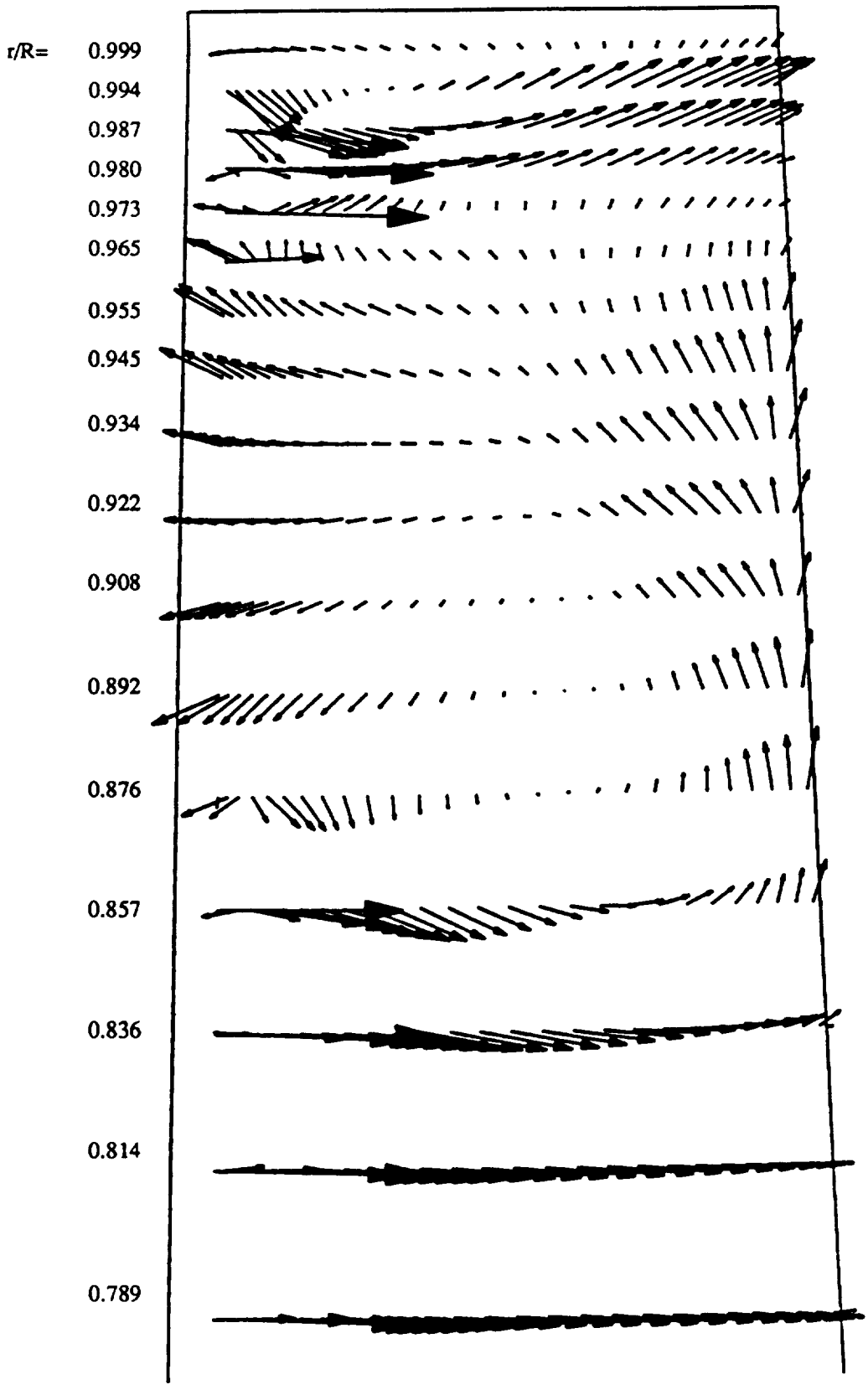

Figure 9. Skin friction vectors for baseline twist, precone=0 deg.

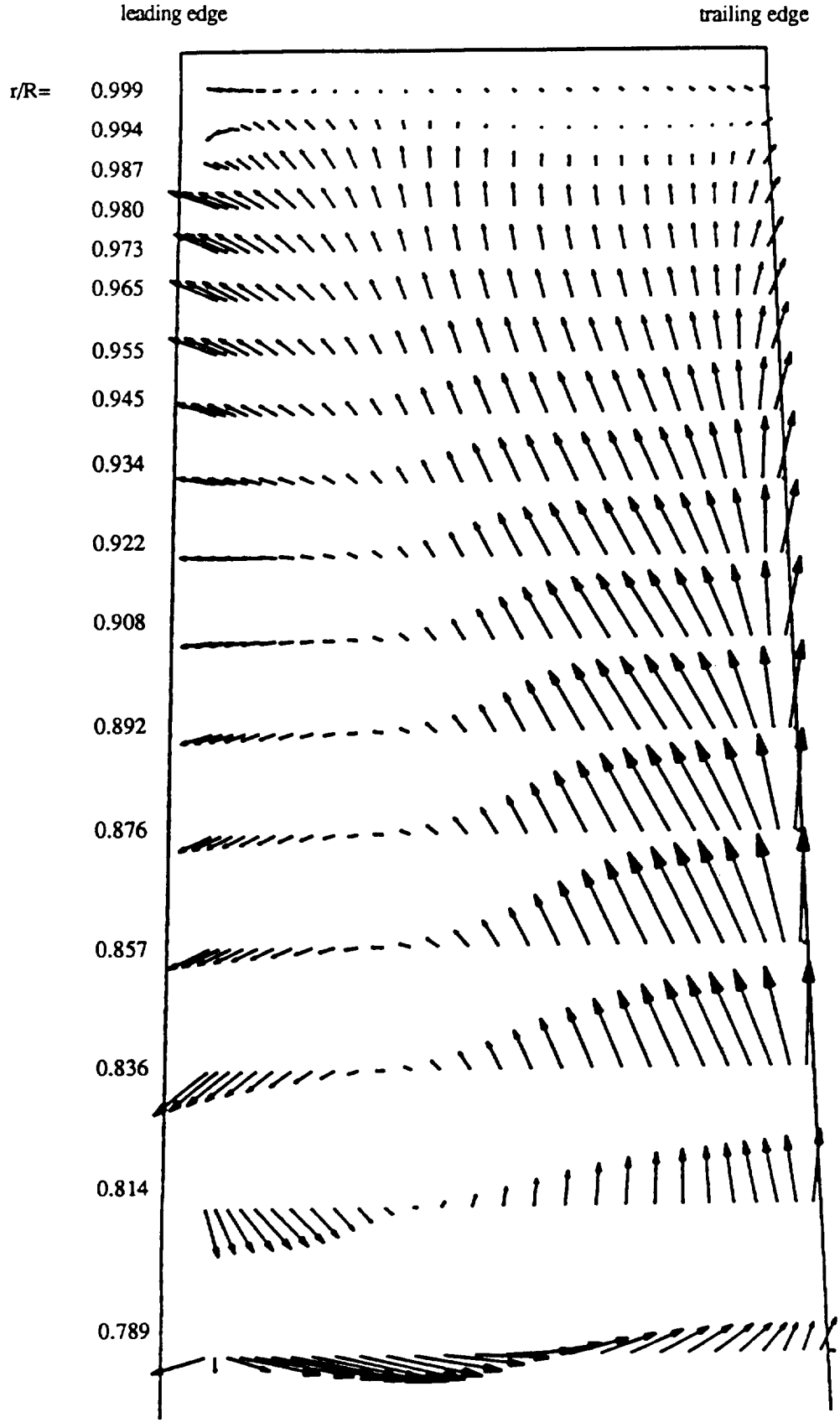

Figure 10. Skin friction vectors for low twist, precone=0 deg.

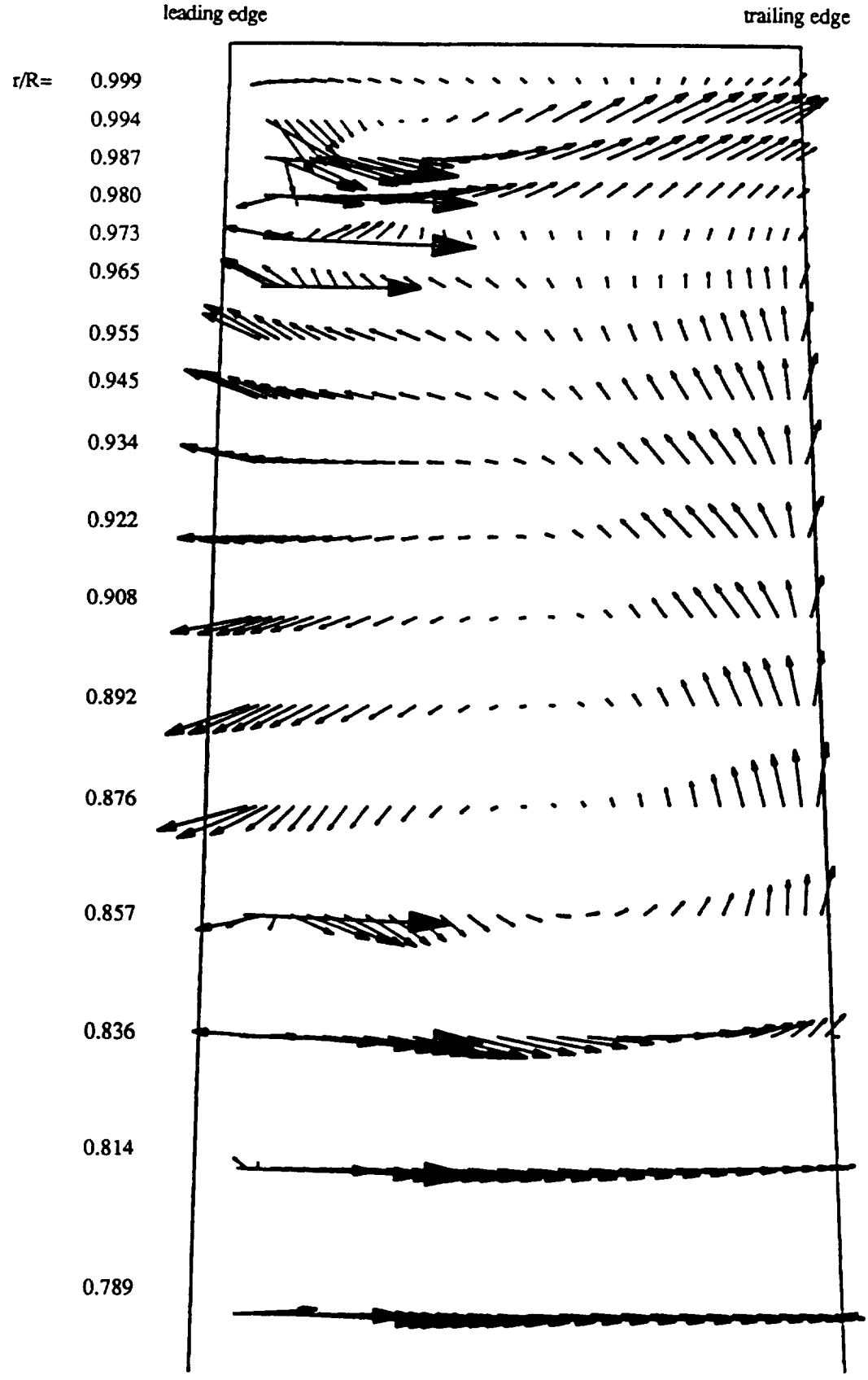

Figure 11. Skin friction vectors for baseline twist, precone=2 deg.

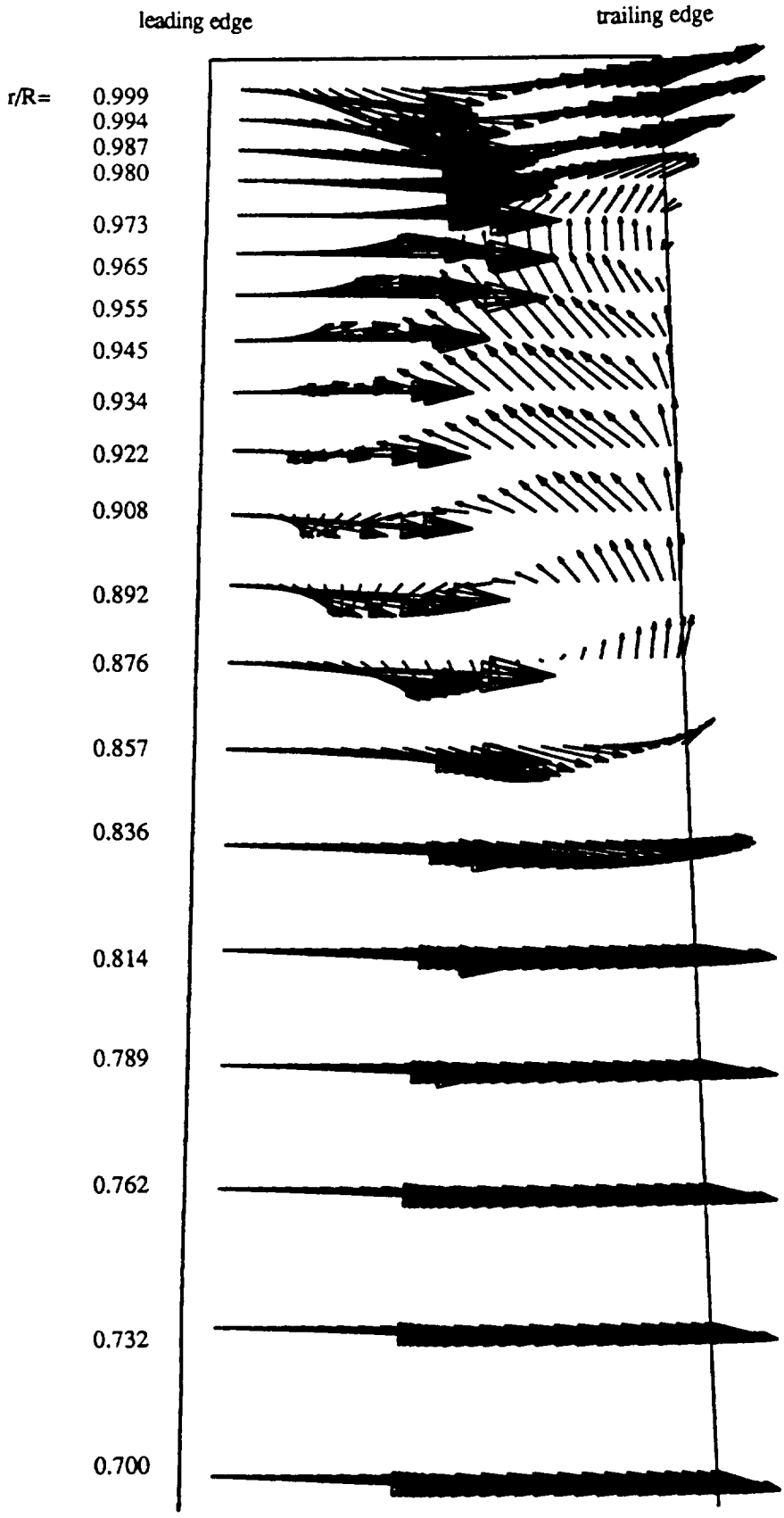

Figure 12. Velocity vectors approximately 0.01 chord above blade (ℓ=20) for baseline twist, precone=0 deg.

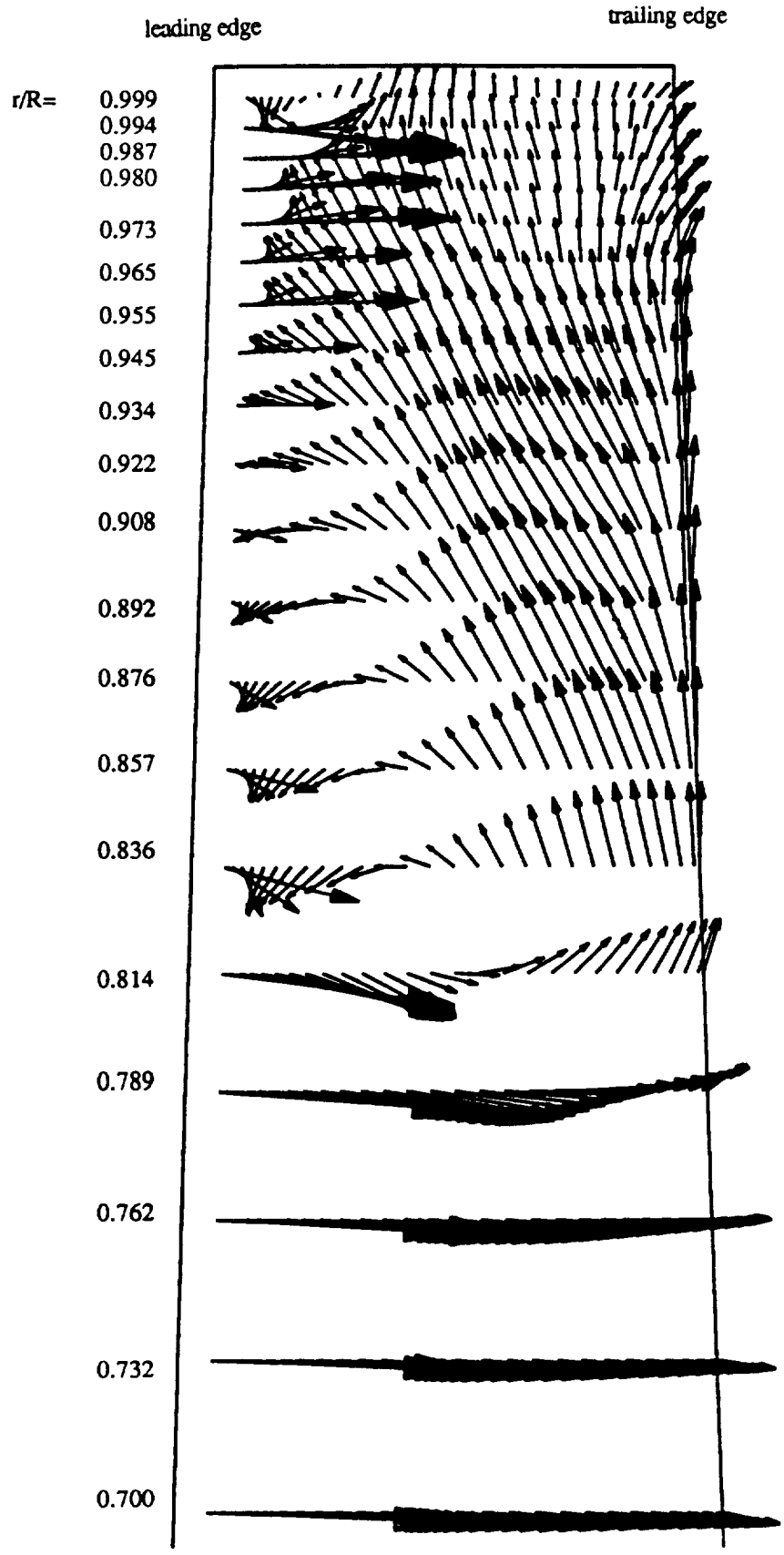

Figure 13. Velocity vectors approximately 0.01 chord above blade (ℓ=20) for low twist, precone=0 deg.

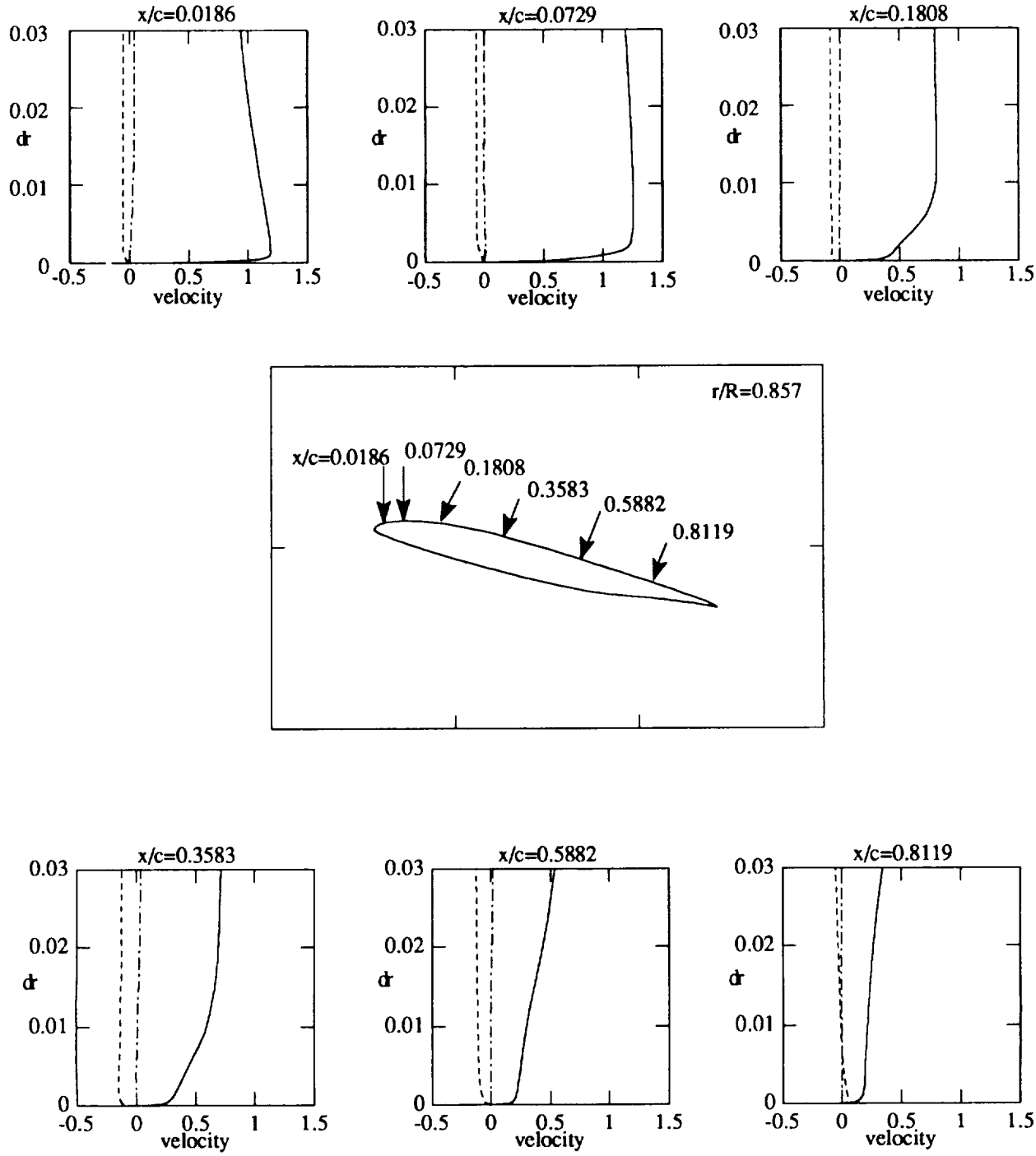

Figure 14. Velocity profiles at r/R=0.857, baseline twist, precone=0 deg, collective=16 deg .
(dr = distance from blade surface, referenced to c_{ref}) ——— u_B-$u_{B\ell=1}$, - - - - - - v_B-$v_{B\ell=1}$,
— - — - w_B-$w_{B\ell=1}$

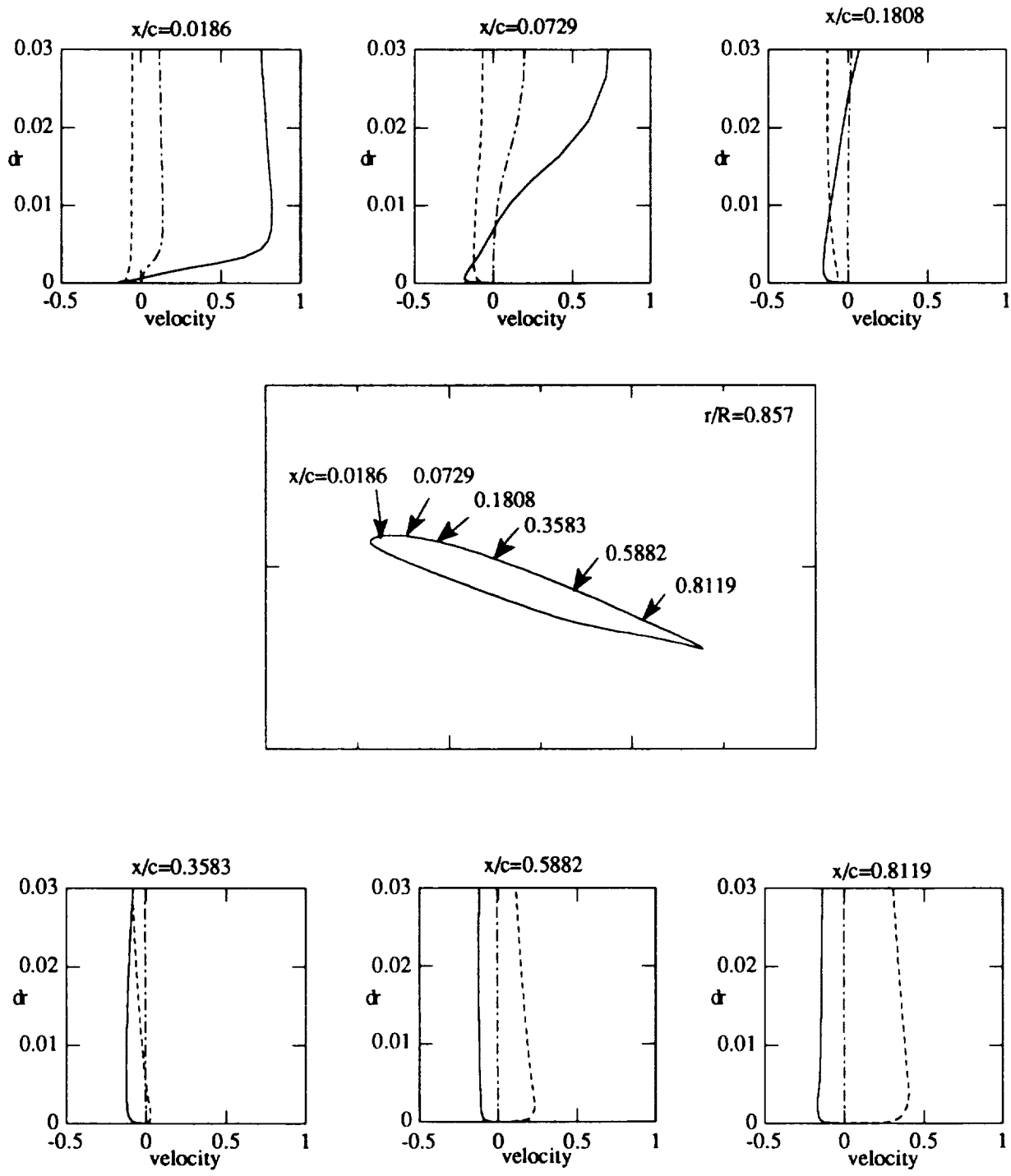

Figure 15. Velocity profiles at r/R=0.857, low twist, precone=0 deg, collective=19 deg (dr = distance from blade surface, referenced to c_{ref}) ——— u_B-$u_{B\ell=1}$, - - - - - - v_B-$v_{B\ell=1}$, — - — - w_B-$w_{B\ell=1}$

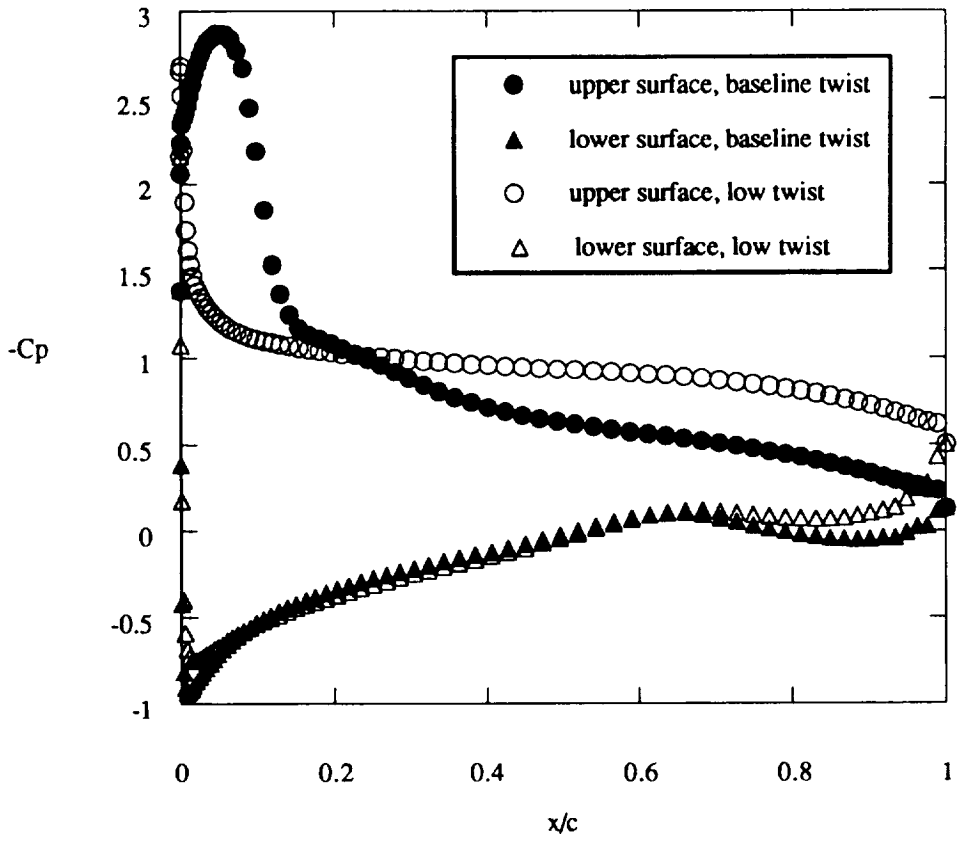

Figure 16. Surface pressure coefficient distribution for baseline and low twist cases (precone=0 deg) at r/R=0.857.

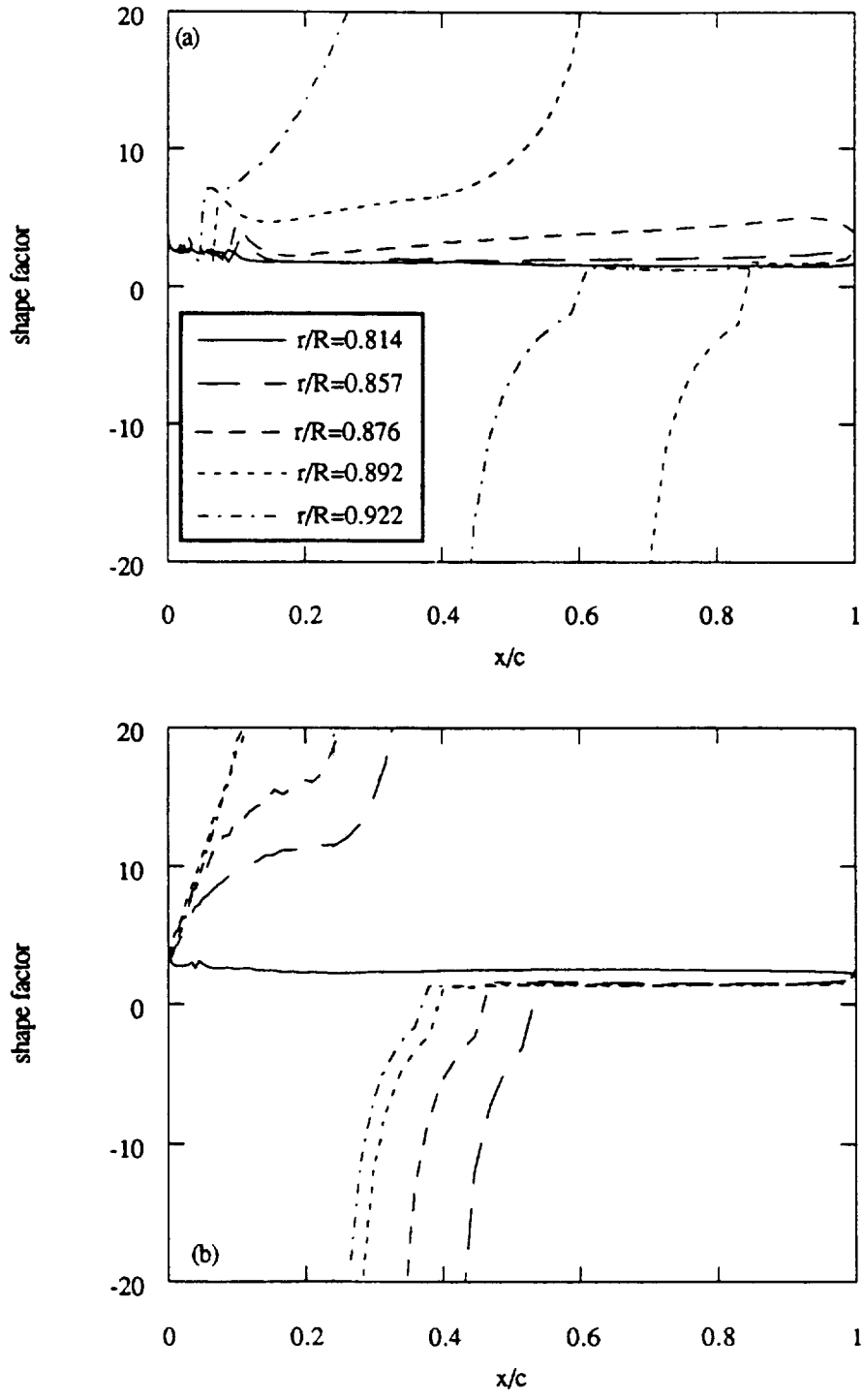

Figure 17. Chordwise shape factor distribution for different spanwise stations. (a) baseline twist, precone=0 deg, (b) low twist, precone=0 deg